ISSN 1998-0124 CN 11-5974/O4
https://doi.org/10.26599/NR.2026.94908667

# Lotus-inspired wood-based evaporation-driven electricity micro-generator

Xu Zeng[1,2], Zheng Wei[1], Yao Tan[1], Sheng-Hong Wu[1], Hai-Tao Deng[3], Yan Wang[1,2], Xiao-Sheng Zhang[1,2](✉)

[1] School of Integrated Circuit Science and Engineering, University of Electronic Science and Technology of China, Chengdu 611731, China

[2] State Key Laboratory of Electronic Thin Films and Integrated Devices, University of Electronic Science and Technology of China, Chengdu 611731, China

[3] CREMeB, Institute of Industrial Science, The University of Tokyo, Tokyo 153-0041, Japan

*Nano Res.*, **Just Accepted Manuscript** • https://doi.org/10.26599/NR.2026.94908667
**https://www.sciopen.com/journal/1998-0124** on Mar. 23, 2026

© The Authors(s)

## Just Accepted

This is a “Just Accepted” manuscript, which has been examined by the peer-review process and has been accepted for publication. A “Just Accepted” manuscript is published online shortly after its acceptance,which is prior to technical editing and formatting and author proofing. Tsinghua University Press (TUP) provides “Just Accepted” as an optional and free service which allows authors to make their results available to the research community as soon as possible after acceptance. After a manuscript has been technically edited and formatted, and the page proofs have been corrected, it will be removed from the “Just Accepted” web site and published officially with volume and article number (e.g., *Nano Research*, **2025**, *18*, 94906990). Please note that technical editing may introduce minor changes to the manuscript text and/or graphics which may affect the content, and all legal disclaimers that apply to the journal pertain. In no event shall TUP be held responsible for errors or consequences arising from the use of any information contained in these “Just Accepted” manuscripts. To cite this anuscript please use its Digital Object Identifier (DOI®),which is identical for all formats of publication.

Just Accepted

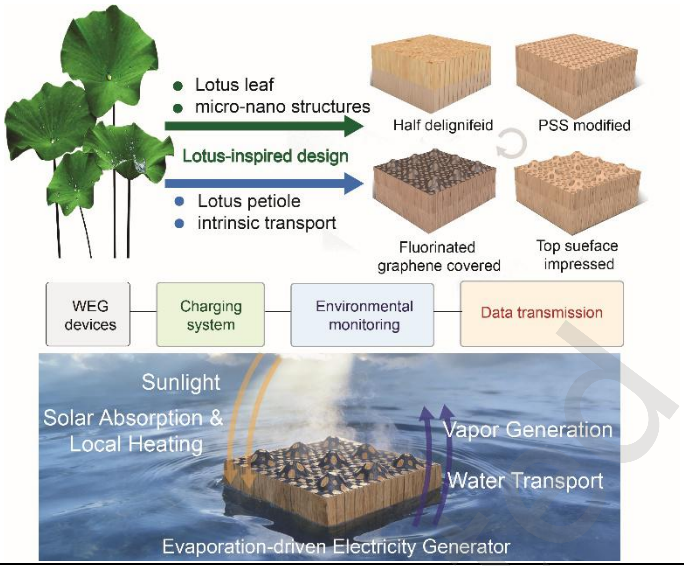

This work presents a lotus-inspired wood-based evaporation-driven electricity generator that couples surface engineering and chemical modification to achieve stable power output.

Nano Research

Open Access

Research Article

# Lotus-inspired wood-based evaporation-driven electricity micro-generator

Xu Zeng[1,2], Zheng Wei[1], Yao Tan[1], Sheng-Hong Wu[1], Hai-Tao Deng[3], Yan Wang[1,2], and Xiao-Sheng Zhang[1,2,]✉
[1] *School of Integrated Circuit Science and Engineering, University of Electronic Science and Technology of China, Chengdu 611731, China*
[2] *State Key Laboratory of Electronic Thin Films and Integrated Devices, University of Electronic Science and Technology of China, Chengdu 611731, China*
[3] *CREMeB, Institute of Industrial Science, The University of Tokyo, Tokyo 153-0041, Japan*

**Received:** 11 January 2026; **Revised:** 18 February 2026; **Accepted:** 23 March 2026

✉Address correspondence to Xiao-Sheng Zhang, email: zhangxs@uestc.edu.cn

**Cite this article:** *Nano Research*, 2026, 19, 94908667 https://doi.org/10.26599/NR.2026.94908667

**ABSTRACT:** Evaporation-driven electricity generation has recently emerged as a promising strategy for harvesting ubiquitous ambient energy. Among various material platforms, wood-based evaporation-driven electricity generators have attracted growing attention owing to their aligned microchannels, intrinsic capillary transport capability, and sustainability. However, the electrical output of unmodified wood remains insufficient to meet the power requirements of practical microsystems. Here, inspired by the architecture of the lotus, we report a bioinspired wood-based evaporation-driven electricity micro-generator with enhanced performance. The hydrophobic micro-nano hierarchical structures of lotus leaves inspire the construction of a microstructured and fluorinated interface on the wood surface to enhance interfacial evaporation. Meanwhile, inspired by the vascular structure of lotus petioles, partial delignification is applied to the bottom region of the wood to enlarge pore channels and establish capillary-Laplace pressure gradients for accelerated water transport. In combination with poly(4-styrenesulfonic acid) (PSS) modification to regulate ionic transport, the resulting device exhibits an approximately 234% increase in output voltage compared with natural wood. Furthermore, assembled devices can be connected in series to charge conventional low-power electronic systems, demonstrating strong potential for autonomous IoT and off-grid micro-energy applications.

**KEYWORDS:** nanogenerator, self-powered, power MEMS, wood electronics

## 1. **Introduction**

The growing global demand for clean and renewable energy has driven the exploration of sustainable energy-harvesting technologies[1-3]. Among various natural energy sources, water represents a vast and largely untapped reservoir of renewable energy. The continuous processes of water evaporation and transport in nature provide a constant flux of energy that can be utilized for electricity generation. Recently, water evaporation-driven electricity generation (WEG) has emerged as a promising approach that converts the energy of natural water evaporation into electrical power[4-7]. This mechanism relies on the directional transport of water molecules and ions within porous materials under ambient conditions[8]. Unlike conventional solar or wind energy systems, WEG can operate continuously as long as a water supply is available, without requiring sunlight or external electrical bias, thereby providing stable and environmentally friendly power output.

Wood has recently attracted increasing attention as a natural and sustainable platform for WEGs[9-11]. Its hierarchical structure, composed of vertically aligned microchannels, facilitates efficient water transport and ion diffusion[12, 13]. The hydrophilic nature of cellulose also enables continuous evaporation under ambient conditions. Several studies have demonstrated the potential of wood-based WEGs[14-18]. For instance, Lin et al. developed a delignified all-wood generator, where lignin removal increased specific surface area, hydrophilicity, and surface charge density, enabling efficient and durable evaporation-driven electricity generation[9]. Zhao et al. developed a Janus evaporator combining cotton hydrogel, hydrophilic polyester fabric, and hydrophobic wood, achieving high solar absorptance and efficient seawater desalination[19]. However, pristine and even modified wood materials still face significant challenges. The intrinsic low electrical conductivity of natural wood results in large internal resistance and limited charge transport efficiency, leading to relatively low output voltage and current compared to other carbon-based or polymer-based WEGs[20, 21]. In addition, the smooth and flat surface of native wood restricts the effective evaporation interface, while its uniform wettability and simple pore geometry hinder the regulation of water flow and potential distribution. Although modification strategies such as carbonization[10, 22], conductive coating[23, 24], and chemical functionalization[11, 25] have been developed, they often fail to promote the interfacial evaporation behavior and dynamic ion transport, limiting the overall energy conversion efficiency of wood-based WEG devices. To further enhance energy conversion, the perspective of biomimetic evaporation and power generation has recently garnered significant attention. Studies have highlighted that constructing nature-inspired hierarchical architectures and optimizing interfacial engineering are critical for maximizing hydrovoltaic performance and evaporation kinetics[26-29].

To address the intrinsic limitations of natural wood, a biomimetic strategy inspired by the lotus was adopted to regulate water evaporation and ion transport. The lotus leaf has a micro-nano hierarchical surface that enables water repellence and efficient vapor release[30, 31]. Following this concept, a Janus wood surface was constructed with asymmetric wettability. The upper surface was coated with fluorinated graphene to create a hydrophobic layer, while the PSS-modified inner wood remained hydrophilic to maintain a continuous water supply. Conical microstructures were imprinted on the surface, resembling the papillae of lotus leaves. These structures enlarge the evaporation area and form multiple light reflection paths, which accelerate the surface evaporation under illumination. In addition, inspired by the aerenchyma architecture in lotus petioles, the internal pores were tailored to form a gradient channel, with larger pores at the bottom and smaller pores at the top. This design generates a Laplace pressure difference that drives water upward[32, 33]. The combined bioinspired and structural strategies enhance water transport, promote ion migration, and improve the overall evaporation-driven power generation of wood-based WEGs. Unlike conventional wood modification, the coordinated optimization of internal water transport and surface evaporation establishes a more efficient capillary flow. Thereby, the hydrovoltaic output was enhanced within a single bioinspired structural framework.

In this work, we developed a lotus-inspired wood-based evaporation-driven micro-generator through ~~a simple~~ process combining synergistically engineered internal channels and asymmetric interfacial functionalization. This biomimetic design enables rapid evaporation and directional water transport through the wood microchannels. As a result, the modified wood exhibits a higher evaporation rate, increased open-circuit voltage (up to 400 mV), and enhanced current output (up to 32 μA) compared with unmodified wood. This study demonstrates that rational surface engineering and biomimetic design can significantly boost the energy conversion efficiency of wood-based WEG systems, achieving a solar-vapor energy efficiency of 67.76%. The proposed device also holds great promise for powering next-generation self-powered micro-systems operating on water surfaces, offering a sustainable route toward intelligent and autonomous hydrovoltaic energy applications.

## 2. Materials and methods

### 2.1 Materials

Balsa wood was cut into 20×20×10 $mm^3$ blocks. Sodium Hydroxide (NaOH) was purchased from Chengdu Aoshuo Biotechnology Co., Ltd., China. Sodium Sulfite ($Na_2SO_3$) was purchased from Shanghai Aladdin Biochemical Technology Co., Ltd., China. Glutaraldehyde was purchased from Chengdu Aoshuo Biotechnology Co., Ltd., China. Poly(4-styrenesulfonic acid) (PSS) was purchased from Shanghai Titan Technology Co., Ltd., China. Fluorinated Graphene was purchased from Shanghai Macklin Biochemical Technology Co., Ltd., China. All chemical reagents were used directly without further purification.

### 2.2 Preparation of gradually delignified wood

A mixed solution of 2.5 mol $L^{-1}$ NaOH and 0.4 mol $L^{-1}$ $Na_2SO_3$ was prepared and heated to boiling on a hot plate. The lower half of the cut balsa wood blocks was immersed in the solution for 4 h, followed by rinsing with deionized water. Since only the lower half of the wood was delignified, the resulting samples exhibited pores that were narrower at the top and wider at the bottom. Finally, the sample was vacuum freeze-dried for 12 hours. Partial delignification selectively removes lignin from the lower region while preserving the cellulose framework, resulting in enlarged lumen channels and reduced hydraulic resistance. This asymmetric pore distribution establishes a vertical gradient in capillary pressure, facilitating directional water transport. The comparison of chemical components before and after delignification is shown in Fig. S1.

### 2.3 Preparation of Janus wood

The gradual-delignified samples were then immersed in a 5 wt% glutaraldehyde solution at 80 °C for 2 h. After rinsing with deionized water, they were immersed in a 5 wt% PSS solution at 70 °C for 2 h for modification, followed by vacuum freeze-drying for 12 h. Then, a 10 mg $mL^{-1}$ fluorinated graphene ethanol solution was prepared and uniformly coated on the surface. Finally, the sample was dried in an oven at 50 °C for 30 min. The Janus modification introduces asymmetric wettability by constructing a hydrophobic upper interface while retaining a hydrophilic interior. This configuration suppresses excessive surface wetting and stabilizes interfacial evaporation. Simultaneously, the fluorinated graphene layer provides broadband photothermal conversion, enhancing surface temperature under illumination and promoting evaporation-driven ion migration.

### 2.4 Preparation of microstructured Janus wood

An aluminum plate with conical array microstructures was fabricated using computer numerical control (CNC) machining. The conical cavities were arranged in a 35×35 array, each with a base radius of 0.25 mm and a height of 1 mm. The microstructures on the aluminum plate were then imprinted onto the hydrophobic side using a tablet press. The conical structures on the mold were engraved inward, forming a negative pattern, which generated corresponding protruding micro-cone arrays on the wood surface after imprinting. During the process, the aluminum template was placed in direct contact with the wood surface and mechanical pressure was applied using the tablet press to ensure uniform structural transfer. Owing to the relatively low hardness and good compressibility of balsa wood, the microstructures could be effectively replicated without structural fracture, enabling complete transfer of the designed surface geometry.

Microstructure imprinting further enhances surface functionality by increasing roughness and inducing light-trapping effects. The conical array geometry reduces optical reflection through multiple internal reflections, thereby improving solar absorption. Additionally, the increased effective surface area strengthens localized evaporation, working synergistically with internal channel regulation and interfacial charge modulation.

### 2.5 Characterization

Scanning electron microscopy (SEM) equipped with energy-dispersive X-ray spectroscopy (JSM-7600F, JEOL) was employed to observe the surface morphology and elemental distribution. The surface zeta potential was measured using a Dynamic light scattering (DLS) zeta potential and nanoparticle size analyzer (Malvern Instruments Ltd., England) to evaluate the surface charge characteristics. Light absorption spectra were obtained using a UV-Vis spectrophotometer (UV-3600, Japan). The surface wettability was assessed by measuring the static water contact angle (CA) with a contact angle goniometer (SDC-100, China). The temperature was monitored with an Infrared thermal imaging camera (UNI-T, China). A vacuum drying oven (PVD-050C, Shanghai Shibei Instrument Equipment Co., Ltd., China) and a freeze dryer (Beijing Songyuan Huaxing Technology Development Co., Ltd.) were introduced to dry the treated wood. The electrical performance of the wood-based WEGs was evaluated under ambient conditions. The output voltage was recorded using a digital multimeter (Keithley 6500, China), and the output current was monitored with an electrometer (Keithley 6514, China). A standard solar simulator (AM 1.5G, 100 mW $\mathrm{cm}^{-2}$) was used to provide illumination when required.

## 3. Results and discussion

### 3.1 Design principle of the wood-based evaporation-driven electricity generator

The design of this wood-based evaporation-driven electricity micro-generator comes from the research on the lotus transpiration mechanism, which is distinct from that of most terrestrial plants (Fig. 1a). Their upper surface contains densely distributed stomata and a micro-nano hierarchical structure covered with a waxy layer, forming a superhydrophobic interface. This structure effectively prevents the accumulation of surface water while maintaining efficient transpiration. Such a combination of directional water transport, stable evaporation, and surface hydrophobicity provides an excellent natural model for designing biomimetic evaporation-driven energy devices with enhanced efficiency and environmental adaptability.

On the basis of the mechanism of the lotus transpiration mechanism, we have designed a wood-based WEG. The WEG was constructed based on a natural wood substrate, serving as a sustainable and porous framework for water and ion transport. The pristine balsa wood was first partially delignified to increase pore size and enhance capillary water flow. The upper and lower surfaces exhibit distinct pore morphologies, as shown in Fig. S2. Subsequently, the samples were modified with PSS solution to improve surface hydrophilicity and charge density. The top surface was then imprinted with an aluminum mold containing conical microarrays to replicate the lotus-leaf-like microstructure, effectively enlarging the evaporation interface. A thin layer of fluorinated graphene was further coated on the microstructured surface to form a hydrophobic upper layer, resulting in a Janus structure with asymmetric wettability. Furthermore, the hydrophobic surface layer functions as an efficient photothermal converter. When the device floats on the water surface under sunlight, the fluorinated graphene coating rapidly absorbs solar energy and increases the surface temperature, thereby enhancing surface water evaporation. (Fig. 1b). Fig. 1c compares the surface microstructures of a natural lotus leaf and the fabricated evaporation-driven device. The lotus leaf (left) exhibits a typical micro-nano hierarchical architecture, while the device surface (right) presents a similarly rough and porous morphology, indicating effective lotus-inspired structural mimicry. Fig. 1d shows the evaporation-induced electrical output of a lotus petiole, exhibiting a stable voltage under ambient condition. Inspired by this natural phenomenon, as illustrated in Fig. 1e, the electricity generation of the wood-based device is driven by the coupling between water evaporation and ion transport along the cellulose microchannels. Continuous evaporation at the top hydrophobic surface induces an upward water flow, carrying solvated ions through the channels and forming an electric double layer along the channel walls. The asymmetric wettability and charge distribution between the top and bottom regions establish a potential gradient, resulting in a measurable voltage output. The PSS-modified hydrophilic region provides abundant negatively charged sulfonate groups ($-SO_3^-$), which facilitate ion migration and charge separation, while the fluorinated graphene layer on the surface enhances evaporation through photothermal heating. Inspired by the architecture of lotus petioles, the conical pore geometry further generates a Laplace pressure difference, where the narrower upper pores and wider lower channels create a capillary force that promotes water transport upward. To understand the driving mechanism of water transport within the gradient wood, we analyze the theoretical capillary pressure distribution based on the pore size evolution. When water fills these interconnected microchannels, the capillary pressure can be described by the Young-Laplace relation:

$$P = \frac{2\gamma cos\theta}{r} \qquad (1)$$

where $\gamma$ is the surface tension of water, $\theta$ is the effective contact angle, and r is the effective pore radius. Due to the difference in pore size, smaller pores in the upper region generate a higher Laplace pressure than the wider channels in the lower region, thereby establishing a pressure gradient along the thickness direction. This gradient provides a continuous driving force that promotes upward water transport from the delignified bottom region toward the upper surface.

Overall, the integration of asymmetric wettability, photothermal enhancement, and Laplace pressure-driven water transport enables efficient ion migration and continuous electricity generation in the wood-based WEG system.

### 3.2 Characterization of the wood-based evaporation-driven electricity generator

The surface microstructure of the wood-based WEGs is illustrated in Fig. 2a. The nano-scale pores on the wood channel walls are shown in Fig. S3. The pristine natural wood (NW) exhibits a smooth and well-aligned cellular channel structure, which facilitates rapid water penetration and results in a low contact angle (CA) of 10°, reflecting its inherent hydrophilicity. After modification with fluorinated graphene, the Janus wood (JW) presents a roughened and disordered pore morphology, and its CA markedly increases to 126°, confirming the successful construction of a hydrophobic surface. Upon further microstructuring by impressing, the microstructured Janus wood (MJW) develops a hierarchical surface architecture composed of microscale protrusions and nanoscale fluorinated domains. Such a dual-scale texture closely resembles the micro/nano composite structures found on natural lotus leaves. Consequently, the MJW exhibits a high CA of 130°, demonstrating the synergistic effect of bionic surface topology and chemical modification on hydrophobic performance. The dynamic wetting behaviors of natural balsa wood, the Janus wood and the microstructured

Janus wood are provided in Fig. S4-6. The wettability of the hydrophobic and hydrophilic sides of the Janus structure is shown in Fig. S7. As shown in Fig. 2b, EDS elemental mapping of MJW confirms the uniform distribution of carbon (C), oxygen (O), and fluorine (F) elements across the surface. The EDS comparison images of the PSS-modified wood are shown in Fig. S8. These results collectively indicate that the MJW successfully integrates a lotus-inspired hierarchical micro/nanostructure with a fluorine-enriched surface chemistry, forming a stable hydrophobic interface that is favorable for efficient evaporation-driven energy conversion. A comprehensive comparison of the surface physicochemical properties is presented in Fig. 2c. The radar chart highlights the distinct variations among NW, JW, and MJW in terms of surface roughness, porosity, zeta potential, contact angle, and optical absorption. First, regarding surface roughness, the imprinted micro-cone structures on MJW markedly increase the surface roughness to ~500 nm, which substantially enlarges the effective evaporation area compared with the relatively flat surfaces of NW and JW. Second, in terms of porosity, partial delignification enlarges the internal pore channels and increases the accessible pore volume within the wood substrate. However, after fluorinated graphene coating and microstructure imprinting, the apparent porosity of JW and MJW shows a slight decrease. This reduction mainly arises from the alternation of the superficial pore morphology. Third, with respect to zeta potential, the surface charge shifts from −29.8 mV for NW to −18.6 mV. Fourth, in terms of surface wettability, MJW exhibits a pronounced transition from the superhydrophilic nature of NW (~0°) to a hydrophobic state with a contact angle of ~130°, which suppresses surface water accumulation and preserves unobstructed vapor diffusion pathways. Finally, from an optical perspective, the solar absorption of MJW increases to ~65%, compared with ~35% for NW, benefiting from the black-body-like photothermal behavior of fluorinated graphene and the light-trapping effect induced by the micro-cone surface geometry. Collectively, the evolution from NW to JW and finally to MJW reveals a systematic performance enhancement, driven by the gradual integration of interfacial regulation and structural optimization. The gradual evolution from hydrophilic NW to hydrophobic JW and finally to hierarchically structured MJW demonstrates that both chemical modification and structural regulation effectively tailor the surface wetting and charge characteristics.

The optical absorption spectra shown in Fig. 2d reveal that fluorinated graphene significantly enhances the broadband light absorption of wood across the 300-2500 nm range. The roughened surface and hierarchical porous architecture of MJW further increase multiple scattering and photothermal conversion efficiency. Such strong light-harvesting capability enables rapid interfacial heating under solar illumination, thereby accelerating water evaporation and enhancing hydrovoltaic output performance. To further verify the surface chemical composition, X-ray photoelectron spectroscopy (XPS) analysis was performed, as shown in Fig. 2e. The survey spectra provide an overview of the elemental composition of the samples. For natural wood (NW), the high-resolution C 1s and O 1s spectra show only typical lignocellulosic signals. In contrast, Janus wood (JW) exhibits clear fluorination features: the C 1s and O 1s spectra reveal new C-F/C-$F_2$ components and reduced oxygen-related peaks, while a distinct F 1s peak at ~688.5 eV confirms the presence of fluorinated species. These results verify the successful anchoring of fluorinated graphene, which forms stable C-F bonds and imparts hydrophobicity to the JW surface. Furthermore, the Raman spectra (Fig. S9) show that JW presents distinct D and G bands, while NW only exhibits weak lignocellulosic signals, confirming carbon-based structural modification on JW.

### 3.3 Output performance of the wood-based evaporation-driven electricity generator

The effect of geometric dimensions and chemical modifications on the evaporation-driven electricity generation was investigated using natural balsa wood blocks of different heights and side lengths. During the measurements, the wood samples were sandwiched between two inert titanium mesh electrodes, and electrical leads were connected to the upper and lower electrodes for voltage and current recording. As presented in Fig. 3a, the output voltage and current strongly depend on the sample height. Both output voltage and current first increase and then decrease with height, reaching a maximum at 10 mm, where the voltage increases to 107 mV and the current reaches 13.3 μA. This trend arises from the trade-off between water transport and internal resistance: thinner samples provide limited evaporation channels, while thicker ones restrict vapor diffusion. In contrast, enlarging the side length (Fig. 3b) continuously enhances output at smaller sizes due to the increased evaporation area and ion transport interface. As the side length increases from 1 to 5 cm, the output voltage rises from 72 mV to 153 mV, and the current increases from about 8 μA to 16 μA. These results indicate that both vertical (height) and lateral (side length) dimensions play critical roles in optimizing the hydrovoltaic performance of wood-based generators. Therefore, wood blocks with dimensions of 2 × 2 × 1 cm were used for all subsequent surface modifications and performance tests.

To further enhance charge transport and interfacial activity, the lower part of the wood samples was subjected to delignification treatment and subsequently modified with poly(sodium 4-styrenesulfonate) (PSS) solutions of different concentrations. The corresponding output voltage and current of PSS-modified wood (PSSW) are shown in Fig. 3c. With increasing PSS concentration, the output voltage increases to 297 mV, while the current rises to 15 μA. Moderate $-SO_3^-$ groups effectively improve interfacial charge transport and enhance the hydrovoltaic output of the wood-based generator. The effect of environmental conditions on the modified wood-based device was further examined (Fig. 3d). The output voltage and current decrease with increasing humidity due to suppressed evaporation, while both increase with temperature owing to enhanced water evaporation and ion transport. All measurements were conducted under controlled conditions, with either temperature or humidity fixed to isolate the effect of the other parameter.

As shown in Fig. S10, repeated sealing causes a rapid voltage drop by blocking interfacial evaporation, whereas unsealing immediately restores the voltage output. This reversible switching further verifies the environmental responsiveness and stability of the device. To further improve the hydrovoltaic output, a lotus-inspired Janus structure was adopted. Fluorinated graphene was coated on the upper surface of the wood to create a hydrophobic layer (JW), and conical microarrays were subsequently imprinted to obtain the final microstructured Janus wood (MJW) device. The JW and MJW produce higher voltage and current than NW and PSSW. Specifically, the MJW delivers an output voltage of approximately 370 mV and a current of about 25 μA When illuminated (JW-L and MJW-L), both devices exhibit a remarkable increase in output (Fig. 3e), with MJW-L reaching nearly 400 mV. To evaluate the operational stability of the wood-based hydrovoltaic device, long-term output measurements were conducted, as illustrated in Fig. 3f. This stable behavior demonstrates the excellent durability of the bioinspired Janus design during prolonged operation. After long-term operation, the surface microstructures and interfacial hydrophobicity of the device remain stable, as evidenced by the characterizations shown in Fig. S11-12. The modified substrate also remains stable after long-term testing (Table S2).

Furthermore, the performance of the MJW device was compared with representative wood-based and hydrovoltaic systems reported in the literature (Fig. 3g)[10, 25, 34-38]. The MJW exhibits both higher voltage and current output, positioning it within the upper-right region of the comparison plot. A more direct tabulated comparison is provided in Table S1. This superior performance can be attributed to the synergistic effects of ionic modification, fluorinated Janus coating, and hierarchical micro/nanostructures that collectively enhance interfacial evaporation and charge separation efficiency.

### 3.4 Photothermal conversion performance of the wood-based evaporation-driven electricity generator

To further investigate the photothermal behavior of the bioinspired wood-based evaporators, the samples were placed on the water surface and irradiated using a solar simulator, while the top-surface temperature was continuously monitored by infrared thermography (Fig. 4a). The NW, JW, and MJW exhibited distinct heating behaviors. As shown in Fig. 4b, the MJW surface temperature increased most rapidly, reaching approximately 32 °C within 15 min, while JW and NW displayed slower heating rates. The superior temperature rise of MJW can be attributed to the synergistic effect of its fluorinated coating and microstructured surface, which improves light absorption and local heat localization. The quantitative temperature evolution was recorded in Fig. 4c. Finite-element simulations were conducted to compare the optical-thermal responses of the NW and the microstructured wood (MW) (Fig. 4d). The NW surface primarily induces random reflection, resulting in limited light absorption and weak heat confinement. In contrast, the engineered micro-conical array promotes multiple reflections, thereby enhancing local absorption and generating a more concentrated thermal field. The corresponding ray-tracing simulation is provided in Fig. S13. The simulated temperature profiles show excellent agreement with the infrared measurements, confirming that the introduced microstructure effectively strengthens photothermal energy localization at the wood-air interface. The water mass change was monitored to assess the evaporation efficiency (Fig. 4e). All samples exhibit an approximately linear mass decrease, indicating stable and continuous interfacial evaporation. Under one-sun illumination, both the Janus wood and the microstructured Janus wood under light display the fastest mass loss, confirming that the combination of the fluorinated coating and the microstructured surface synergistically accelerates interfacial evaporation. For comparison, bare water under 1 sun shows only a moderate mass decrease, whereas water without illumination exhibits the smallest change (Fig. S14). After one hour of solar illumination, MJW reaches an evaporation rate of approximately $4.3\ \mathrm{kg\ m^{-2}\ h^{-1}}$, whereas JW and NW exhibit rates of about $3.7\ \mathrm{kg\ m^{-2}\ h^{-1}}$ and $2.9\ \mathrm{kg\ m^{-2}\ h^{-1}}$, respectively (Fig. 4f). These results confirm that the bioinspired microstructuring strategy markedly improves interfacial evaporation efficiency under solar irradiation. Furthermore, the water evaporation energy flux density ($E_{evap}$) and the solar-vapor energy efficiency ($\eta_{evap}$) were calculated for each sample based on the Eq. (1-2) below.

$$E_{evap} = m_{evap} \cdot (h_{lv} + c(T_v - T_1)) \qquad (2)$$

$$\eta_{evap} = \frac{E_{evap}}{E_{light}} \times 100\% \qquad (3)$$

Where $m_{evap}$ is the evaporation rate, $h_{lv}$ is the latent heat of vaporization of liquid water, whose magnitude depends on temperature, *c* is the specific heat capacity of liquid water, $T_v$ is the vapor temperature and $T_1$ is the liquid water temperature. $E_{light}$ is the simulated solar energy flux density.

The three samples exhibit distinct energy flux outputs under one-sun illumination. MJW delivers the highest $E_{evap}$, reaching $67.76\ \mathrm{W{\cdot}m^{-2}}$, whereas JW and NW show markedly lower values of $37.05\ \mathrm{W{\cdot}m^{-2}}$ and $20.43\ \mathrm{W{\cdot}m^{-2}}$, respectively (Fig. 4g). The enhanced energy flux of MJW can be attributed to the photothermal behavior and the surface microstructuring, which together increase photothermal conversion and sustain rapid water transport. During the solar-driven evaporation process, in addition to the energy consumed for water vaporization, heat transfer from the illuminated surface to the liquid water and the sensible heating of the liquid before evaporation also contribute to the overall energy consumption. It inherently includes unavoidable thermal losses and thus cannot reach 100%.

### 3.5 Scaling up output performance and its application as an energy source

To evaluate the feasibility of the wood-based WEG as a power supply, the output voltage and current were measured under various external resistances. As shown in Fig. 5a, with the increase of the resistance value, the voltage and current increase and decrease, respectively. This inverse dependence between voltage and current is consistent with typical internal impedance-dominated generators. The corresponding output power (Fig. 5b) exhibits a well-defined peak at an external resistance of approximately $10^4\ \Omega$. At this matched condition, the device delivers the maximum power of 0.29 μW, while both lower and higher resistance values lead to reduced power output. The peak power output of the evaporation-driven generator with heterogeneous electrodes is shown in Fig. S15. The output of the wood-based WEG was further evaluated by electrically integrating multiple units. As shown in Fig. 5c, connecting devices in series leads to a stepwise increase in voltage, reaching approximately 1.2 V with four units. In contrast, parallel connection (Fig. 5d) results in a proportional rise in output current, enabling flexible integration for practical low-power applications. The direct-current output of the wood-based hydrovoltaic device enables capacitor charging without the need for any rectification circuitry. As shown in Fig. 5e, capacitors with different capacitances (100 pF-47 nF) are all charged smoothly to a stable voltage within tens of seconds, demonstrating the device's inherently compatible DC output. Furthermore, the charged voltage increases proportionally when multiple capacitors are connected (Fig. 5f), confirming that the harvested evaporation-induced electricity can be directly accumulated and stored in conventional capacitive elements for subsequent use. In Fig. 5g, four wood-based evaporation-powered generators were connected in series to form a compact power unit. The combined output was capable of charging a small rechargeable battery. Building on this foundation, Fig. 5h presents the evaporation-powered sensor node, where the charged battery reliably drives a temperature-humidity sensing module. The integrated system enables continuous acquisition and wireless transmission of environmental data, demonstrating that the harvested evaporation energy is sufficient to sustain real-time sensing. Beyond wireless sensing, the generator can also directly power small electronic devices, such as a calculator (Supplementary Video 1) and a digital clock (Fig. S16). These results underscore the promise of wood-based WEGs as viable power sources for self-sustained electronic devices.

## 4. Conclusions

In this work, we developed a wood-based evaporation-powered micro-generator that leverages the intrinsic microchannels and substrate tunability of natural wood to achieve efficient interfacial evaporation and stable electricity generation. By introducing combined structural, chemical, and surface engineering strategies, the device exhibited significantly enhanced evaporation rates and electrical output under ambient and solar-irradiated conditions. The modular design further enabled voltage scaling through series integration, allowing the harvested energy to be directly accumulated in conventional capacitors and rechargeable batteries. Overall, these results establish engineered wood as a promising framework for translating ambient evaporation into electrical signals, broadening its utility in self-powered IoT devices, environmental sensing, and related low-power technologies.

**Electronic Supplementary Material:** Supplementary material (please provide the brief detail of the ESM) is available in the online version of this article at https://doi.org/10.26599/NR.2026.94908667.

## Data availability

The data that support the findings of this study are available from the corresponding author upon reasonable request.

## Acknowledgements

This work was supported by the National Natural Science Foundation of China (Grant No. T2541035), the National Key Research and Development Program of China (Grant No.2022YFB3206100), the Fundamental Research Funds for the Central Universities (No. ZYGX2025TS008), the Key R&D Program of Mianyang City (Grant No. 2023ZYDF019), and the Natural Science Foundation of Sichuan Province (Grant No. 2024ZYD0166)

## Declaration of competing interest

Authors declare that they have no competing interests.

## Author contribution statement

Xu Zeng: Investigation, experimental design, data curation, validation, writing manuscript. Zheng Wei: Data curation, validation. Yao Tan: Investigation, visualization. Sheng-Hong Wu: Investigation. Hai-Tao Deng: Visualization. Yan Wang: Investigation. Xiao-Sheng Zhang: Conceptualization, investigation, review & editing, project administration, supervision. All the authors have approved the final manuscript.

## Informed consent

Not applicable.

## Ethics statement

Not applicable.

## Use of AI statement

None.

## References

(1) Ryu, H.; Yoon, H. J.; Kim, S. W. Hybrid Energy Harvesters: Toward Sustainable Energy Harvesting. *Advanced Materials* **2019**, *31* (34). DOI: 10.1002/adma.201802898.

(2) Zou, Y.; Tan, P. C.; Shi, B. J.; Ouyang, H.; Jiang, D. J.; Liu, Z.; Li, H.; Yu, M.; Wang, C.; Qu, X. C.; et al. A bionic stretchable nanogenerator for underwater sensing and energy harvesting. *Nature Communications* **2019**, *10*. DOI: 10.1038/s41467-019-10433-4.

(3) Chen, B. D.; Wang, Z. L. Toward a New Era of Sustainable Energy: Advanced Triboelectric Nanogenerator for Harvesting High Entropy Energy. *Small* **2022**, *18* (43). DOI: 10.1002/smll.202107034.

(4) Tian, Z.; Chang, Q.; Liu, Z.; Xue, C.; Li, N.; Jia, S.; Fan, X.; Yang, J.; Hu, S. Electricity Harvesting from Water Evaporation on Hierarchical Pore Gradient Silica Aerogel-Based Generators. *ACS Applied Materials & Interfaces* **2024**, *16* (32), 42468-42475. DOI: 10.1021/acsami.4c07729.

(5) Hu, Y.; Yang, W.; Wei, W.; Sun, Z.; Wu, B.; Li, K.; Li, Y.; Zhang, Q.; Xiao, R.; Hou, C.; et al. Phyto-inspired sustainable and high-performance fabric generators via moisture absorption-evaporation cycles. *Science Advances* **2024**, *10* (2), eadk4620. DOI: doi:10.1126/sciadv.adk4620.

(6) Xue, G.; Xu, Y.; Ding, T.; Li, J.; Yin, J.; Fei, W.; Cao, Y.; Yu, J.; Yuan, L.; Gong, L.; et al. Water-evaporation-induced electricity with nanostructured carbon materials. *Nature Nanotechnology* **2017**, *12* (4), 317-321. DOI: 10.1038/nnano.2016.300.

(7) Ding, T.; Liu, K.; Li, J.; Xue, G.; Chen, Q.; Huang, L.; Hu, B.; Zhou, J. All-Printed Porous Carbon Film for Electricity Generation from Evaporation-Driven Water Flow. *Advanced Functional Materials* **2017**, *27* (22), 1700551. DOI: https://doi.org/10.1002/adfm.201700551.

(8) Yun, T. G.; Bae, J.; Rothschild, A.; Kim, I.-D. Transpiration Driven Electrokinetic Power Generator. *ACS Nano* **2019**, *13* (11), 12703-12709. DOI: 10.1021/acsnano.9b04375.

(9) Lin, J.; Zhang, Z.; Lin, X.; Cai, X.; Fu, S.; Fang, X.; Ding, Y.; Wang, X.; Sèbe, G.; Zhou, G. All Wood-Based Water Evaporation-Induced Electricity Generator. *Advanced Functional Materials* **2024**, *34* (30), 2314231. DOI:

https://doi.org/10.1002/adfm.202314231.

(10) Zhang, Z.; Zheng, Y.; Jiang, N.; Hong, W.; Liu, T.; Jiang, H.; Hu, Y.; Li, C. Electricity generation from water evaporation through highly conductive carbonized wood with abundant hydroxyls. *Sustainable Energy & Fuels* **2022**, *6* (9), 2249-2255, 10.1039/D2SE00309K. DOI: 10.1039/D2SE00309K.

(11) Ding, Y.; Li, S.; Tian, J.; Wang, F.; Shi, Y.; Tao, X.; Wang, X.; Lei, R.; Chen, X. CNTs/Wood Composite Nanogenerator for Producing Both Steam and Electricity. *ACS Applied Electronic Materials* **2021**, *3* (12), 5287-5295. DOI: 10.1021/acsaelm.1c00796.

(12) Zhu, H.; Luo, W.; Ciesielski, P. N.; Fang, Z.; Zhu, J. Y.; Henriksson, G.; Himmel, M. E.; Hu, L. Wood-Derived Materials for Green Electronics, Biological Devices, and Energy Applications. *Chemical Reviews* **2016**, *116* (16), 9305-9374. DOI: 10.1021/acs.chemrev.6b00225.

(13) Jiang, F.; Li, T.; Li, Y.; Zhang, Y.; Gong, A.; Dai, J.; Hitz, E.; Luo, W.; Hu, L. Wood-Based Nanotechnologies toward Sustainability. *Advanced Materials* **2018**, *30* (1), 1703453. DOI: https://doi.org/10.1002/adma.201703453.

(14) Wong, M. Y.; Gautam, A.; Lin, K. X.; Chen, J. H.; Ho, T. C.; Fahim, M.; Chen, X.; Pan, A. Q.; Tso, C. Y. Sustainable high-performance density-nanoporous composite wood for water evaporation-induced electricity generation. *Chemical Engineering Journal* **2025**, *510*. DOI: 10.1016/j.cej.2025.161729.

(15) Kong, H. R.; Li, Y. T.; Yan, J.; Liu, X.; Xiang, M. X.; Wang, Q. H.; Wang, Y. Enhancing electricity generation from water evaporation through cellulose-based multiscale fibers network. *Chemical Engineering Journal* **2024**, *498*. DOI: 10.1016/j.cej.2024.155872.

(16) Piao, X. X.; Zhang, P.; Shen, J. Y.; Jin, C. D.; Wang, J.; Wang, Z. Water-evaporation induced electricity generation inspired by natural tree transpiration. *Sustainable Materials and Technologies* **2024**, *39*. DOI: 10.1016/j.susmat.2024.e00836.

(17) Han, C. L.; Bai, Z. Q.; Sun, H. H.; Mi, L. T.; Sun, Z. Z. Bioinspired gradient-structured wood interfaces achieving efficient ion diffusion to generate electricity from natural evaporation. *Journal of Materials Chemistry A* **2024**, *12* (2), 723-730. DOI: 10.1039/d3ta05986c.

(18) Li, H. R.; Fan, R. C.; Zhang, F. D.; Cui, Z. W.; Wu, T. T.; Huang, Q.; Kang, F. Y.; Cai, Y. H.; Zhang, Q. C.; Tian, D. Engineering wood-MOF networks to realize multilevel weak water interactions for highly-efficient solar water-power cogeneration. *Chemical Engineering Journal* **2025**, *509*. DOI: 10.1016/j.cej.2025.161332.

(19) Zhao, Z.; Wang, J.; Yu, S.; Qi, Z.; Sun, Z.; Zhang, X. Assembled Wood-Polyester Fabric-Hydrogel Janus Evaporator for Sustainable Seawater Desalination. *ACS Applied Materials & Interfaces* **2024**, *16* (36), 48470-48480. DOI: 10.1021/acsami.4c08345.

(20) Liu, C. R.; Wang, Z.; Tong, X.; Wu, Z. H.; Zhou, L.; Zou, H. Y.; Ogunjuyibe, A.; Lin, H. J.; Yan, D. F.; Yang, W. H.; et al. Water-evaporation-induced direct current electricity generation based on stretchable hydrogel/Al2O3. *Matter* **2025**, *8* (10). DOI: 10.1016/j.matt.2025.102200.

(21) He, N.; Wang, H.; Zhang, H.; Jiang, B.; Tang, D.; Li, L. Ionization Engineering of Hydrogels Enables Highly Efficient Salt-Impeded Solar Evaporation and Night-Time Electricity Harvesting. *Nano-Micro Letters* **2023**, *16* (1), 8. DOI: 10.1007/s40820-023-01215-1.

(22) Chen, J.; Jian, M.; Yang, X.; Xia, X.; Pang, J.; Qiu, R.; Wu, S. Highly Effective Multifunctional Solar Evaporator with Scaffolding Structured Carbonized Wood and Biohydrogel. *ACS Applied Materials & Interfaces* **2022**, *14* (41), 46491-46501. DOI: 10.1021/acsami.2c11399.

(23) Zhang, M.; Shi, L.; Du, X.; Li, Z.; Shi, Y.; An, C.; Li, J.; Wang, C.; Shi, J. Janus mesoporous wood-based membrane for simultaneous oil/water separation, aromatic dyes removal, and seawater desalination. *Industrial Crops and Products* **2022**, *188*, 115643. DOI: https://doi.org/10.1016/j.indcrop.2022.115643.

(24) Piao, X.; Zhang, P.; Shen, J.; Jin, C.; Wang, J.; Wang, Z. Water-evaporation induced electricity generation inspired by natural tree transpiration. *Sustainable Materials and Technologies* **2024**, *39*, e00836. DOI: https://doi.org/10.1016/j.susmat.2024.e00836.

(25) Zhou, X.; Zhang, W.; Zhang, C.; Tan, Y.; Guo, J.; Sun, Z.; Deng, X. Harvesting Electricity from Water Evaporation through Microchannels of Natural Wood. *ACS Applied Materials & Interfaces* **2020**, *12* (9), 11232-11239. DOI: 10.1021/acsami.9b23380.

(26) Chen, C.; Kuang, Y.; Hu, L. Challenges and Opportunities for Solar Evaporation. *Joule* **2019**, *3* (3), 683-718. DOI: https://doi.org/10.1016/j.joule.2018.12.023.

(27) Liu, S.; Liu, X.; Zhou, G.; Qin, F.; Jing, M.; Li, L.; Song, W.; Sun, Z. A high-efficiency bioinspired photoelectric-electromechanical integrated nanogenerator. *Nature Communications* **2020**, *11* (1), 6158. DOI: 10.1038/s41467-020-19987-0.

(28) Wang, W.; Han, C.; Xu, D.; Sun, H.; Sun, R.; Qin, F.; Wu, H.; Sun, Z. Anisotropic surface inspired by reed leaves for water droplet energy harvesting. *Chemical Engineering Journal* **2026**, *529*, 172661. DOI: https://doi.org/10.1016/j.cej.2026.172661.

(29) Han, C.; Bai, Z.; Sun, H.; Mi, L.; Sun, Z. Bioinspired gradient-structured wood interfaces achieving efficient ion diffusion to generate electricity from natural evaporation. *Journal of Materials Chemistry A* **2024**, *12* (2), 723-730, 10.1039/D3TA05986C. DOI: 10.1039/D3TA05986C.

(30) Cheng, S.; Yu, Z.; Lin, Z.; Li, L.; Li, Y.; Mao, Z. A lotus leaf like vertical hierarchical solar vapor generator for stable and efficient evaporation of high-salinity brine. *Chemical Engineering Journal* **2020**, *401*,

126108. DOI: https://doi.org/10.1016/j.cej.2020.126108.

(31) Ensikat, H. J.; Ditsche-Kuru, P.; Neinhuis, C.; Barthlott, W. Superhydrophobicity in perfection: the outstanding properties of the lotus leaf. *Beilstein Journal of Nanotechnology* **2011**, *2*, 152-161. DOI: https://doi.org/10.3762/bjnano.2.19.

(32) Bourgade, M.; Bain, N.; Vanel, L.; Leocmach, M.; Barentin, C. Capillary and priming pressures control the penetration of yield-stress fluids through non-wetting 2D meshes. *Soft Matter* **2025**, *21* (42), 8140-8147, 10.1039/D5SM00759C. DOI: 10.1039/D5SM00759C.

(33) Cai, J.; Chen, Y.; Liu, Y.; Li, S.; Sun, C. Capillary imbibition and flow of wetting liquid in irregular capillaries: A 100-year review. *Advances in Colloid and Interface Science* **2022**, *304*, 102654. DOI: https://doi.org/10.1016/j.cis.2022.102654.

(34) Li, X.; Zhang, K.; Nilghaz, A.; Chen, G.; Tian, J. A green and sustainable water evaporation-induced electricity generator with woody biochar. *Nano Energy* **2023**, *112*, 108491. DOI: https://doi.org/10.1016/j.nanoen.2023.108491.

(35) Li, Z.; Chen, D.; Gao, H.; Xie, H.; Yu, W. Reduced graphene oxide composite nanowood for solar-driven interfacial evaporation and electricity generation. *Applied Thermal Engineering* **2023**, *223*, 119985. DOI: https://doi.org/10.1016/j.applthermaleng.2023.119985.

(36) Lu, W.; Jiang, D.; Wang, Z.; Zhang, X.; Ding, Q.; Zhang, Z.; Liu, X.; Bai, L.; Li, Z.; Liu, Y. Simultaneous efficient evaporation and stable electricity generation enabled by a wooden evaporator based on composite photothermal effect. *Chemical Engineering Journal* **2024**, *496*, 154361. DOI: https://doi.org/10.1016/j.cej.2024.154361.

(37) Ma, C.; An, X.; Guo, M. Superior anti-fouling Janus wood-based evaporator simultaneously achieving efficient evaporation and stable thermoelectric generation. *Journal of Cleaner Production* **2025**, *524*, 146513. DOI: https://doi.org/10.1016/j.jclepro.2025.146513.

(38) Jing, M.; Wang, W.; Fu, Y.; Yang, Y.; Song, W.; Sun, Z. A simple, natural 3D honeycomb structure achieving high photothermal conversion and sustainable salt-resistance for efficient desalination and potential electricity generation. *Desalination* **2023**, *564*, 116792. DOI: https://doi.org/10.1016/j.desal.2023.116792.

## FIGURES.

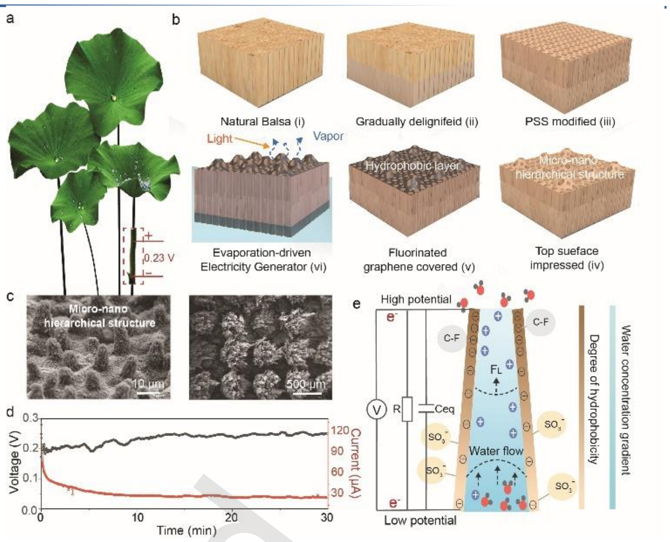

Figure 1. Overview of the lotus-inspired microstructured Janus wood and its water-evaporation-induced electricity generation mechanism. (a) Biological inspiration from the lotus, featuring hierarchical microstructures on the surface and intrinsic water and ion transport pathways within the petiole. (b) Fabrication process of the Janus wood: (i) natural balsa, (ii) gradually delignified wood, (iii) PSS-modified wood, (iv) embossed microstructured top surface, and (v) fluorinated-graphene hydrophobic coating. (vi) Schematic illustration of the complete water-evaporation-induced electricity generator. (c) SEM images of the micro/nano-hierarchical surface structures of a natural lotus leaf (left) and the evaporation-driven electricity generator (right). (d) The output voltage and current generated from the lotus petiole during continuous evaporation-driven operation. (e) Schematic illustration of the working mechanism. The tapered microchannels (narrow top and wider bottom) create a Laplace-pressure-driven upward water transport that accelerates interfacial evaporation. The sulfonate groups on the cellulose pore walls further enhance the electrical output. Meanwhile, the hydrophobic surface layer strengthens photothermal absorption and promotes rapid evaporation at the upper interface.

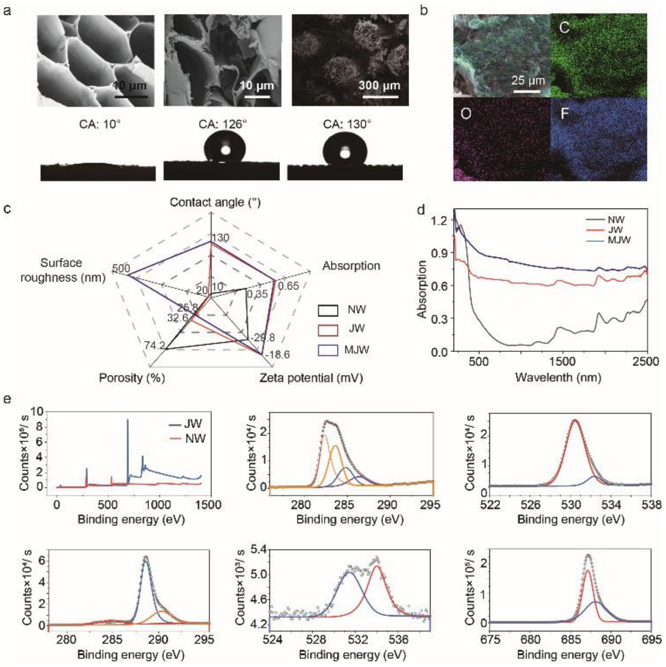

Figure 2. Structural, compositional, and interfacial properties of wood samples. (a) SEM images of NW, JW, and MJW showing the evolution from native cell-wall morphology to embossed microstructured surfaces, together with corresponding water contact angles demonstrating the transition from hydrophilic behavior (CA: 10°) to highly hydrophobic surfaces (CA: 130°). (b) Elemental mapping (C, O, F) of the fluorinated-graphene-coated surface, confirming the uniform distribution of the hydrophobic modification layer.

(c) Radar chart comparing key surface parameters of the three wood types, including contact angle, absorption, zeta potential, porosity, and nanoscale roughness. (d) UV-vis-NIR absorption spectra showing that Janus wood and microstructured Janus wood exhibit markedly enhanced broadband absorption compared with natural wood. (e) XPS analysis: (i) full survey spectra of NW and JW; high-resolution spectra of (ii) C 1s, (iii) O 1s for NW; and (iv–vi) C 1s, O 1s, and F 2p for JW, evidencing successful PSS modification and the introduction of sulfonate functional groups.

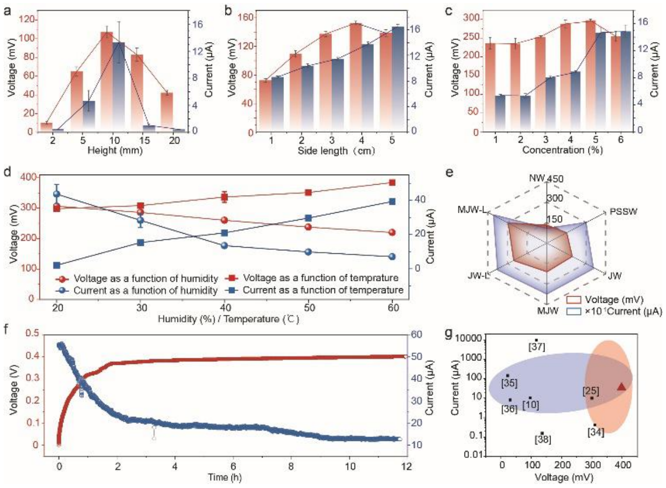

Figure 3. The electrical output performance of the wood-based water evaporation-driven electricity generator. Voltage and current outputs of unmodified natural wood blocks with (a) different heights and (b) side lengths. (c) Electrical performance of wood samples modified with different PSS concentrations, demonstrating the influence of surface charge density on the evaporation-induced output. Effects of environmental conditions, including (d) relative humidity and temperature on the voltage and current outputs. (e) Comparison of various sample configurations, including natural wood (NW), PSS-modified wood (PSSW), Janus wood (JW), microstructured Janus wood (MJW), and their light-irradiated counterparts (JW-L and MJW-L). (f) Long-term stability test of continuous voltage and current output. (g) Comparison of the present device with previously reported hydrovoltaic systems.

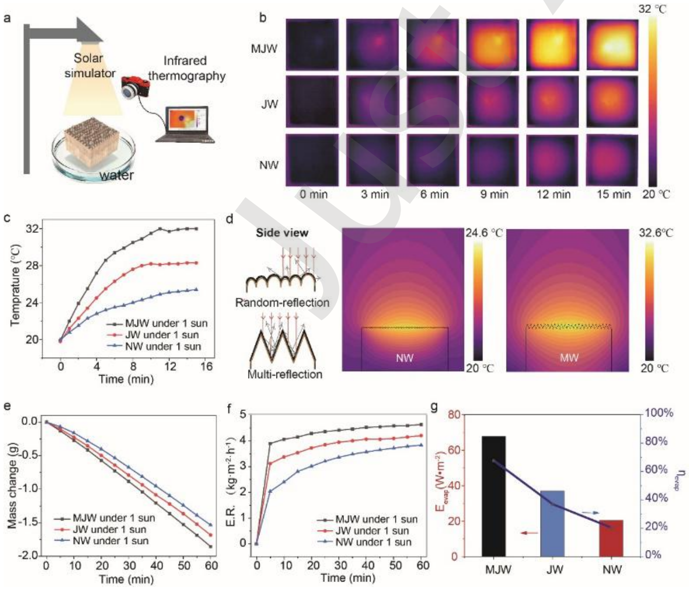

Figure 4. Evaporation performance of natural wood (NW), Janus wood (JW), and microstructured Janus wood (MJW). (a) Experimental setup for photothermal characterization under 1-sun irradiation, with infrared thermography used to monitor the surface temperature of wood-based samples floating on water. (b) Infrared thermographs reveal faster surface heating and higher temperatures for MJW compared with JW and NW under 1-sun illumination. (c) Temperature-time curves of the three kinds of devices. (d) Schematic illustration and COMSOL simulation comparing light behavior on natural wood (random reflection) and microstructured wood (multi-reflection). (e) Mass change curves of water under 1-sun illumination with different wood samples. (f) Corresponding evaporation rates (E.R.). (g) Comparison of the water evaporation energy flux density ($E_{evap}$) and the solar-vapor energy efficiency ($\eta_{evap}$).

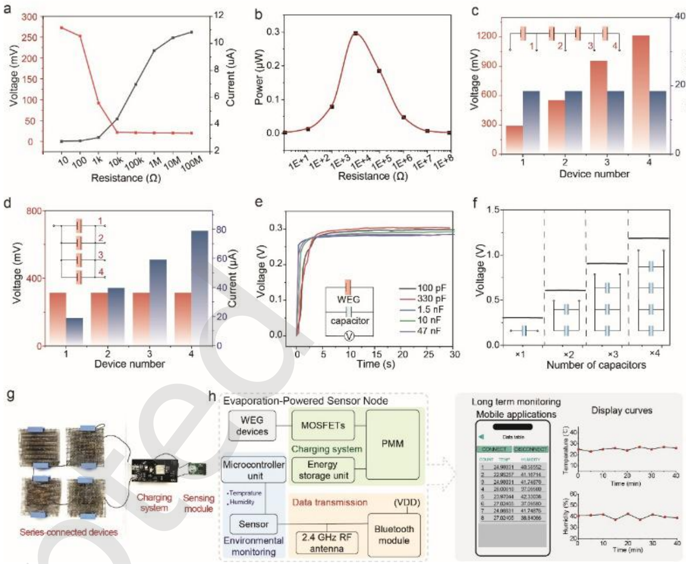

Figure 5. The assembly and application of the wood-based evaporation-driven electricity generator. (a) Load-dependent voltage and current outputs. (b) Corresponding output power curve under various resistances, indicating the optimal resistance for efficient energy extraction. Voltage and current outputs of multiple units connected (c) in series and (d) in parallel. (e) Direct charging of capacitors with different capacitances (100 pF-47 nF). (f) Stepwise increase in stored voltage with multiple capacitors connected, confirming effective accumulation of evaporation-induced electricity. (g) Photograph of four WEG devices connected in series to charge a rechargeable battery, which subsequently powers an external sensing module. (h) Schematic of the evaporation-powered sensor node and demonstration of long-term temperature–humidity monitoring enabled by the charged battery.

# Electronic Supplementary Material

# Lotus-inspired wood-based evaporation-driven electricity micro-generator

Xu Zeng[1,2], Zheng Wei[1], Yao Tan[1], Sheng-Hong Wu[1], Hai-Tao Deng[3], Yan Wang[1,2], and Xiao-Sheng Zhang[1,2,]✉

[1] *School of Integrated Circuit Science and Engineering, University of Electronic Science and Technology of China, Chengdu 611731, China*

[2] *State Key Laboratory of Electronic Thin Films and Integrated Devices, University of Electronic Science and Technology of China, Chengdu 611731, China*

[3] *CREMeB, Institute of Industrial Science, The University of Tokyo, Tokyo 153-0041, Japan*

✉Address correspondence to Xiao-Sheng Zhang, email: zhangxs@uestc.edu.cn

Supporting information to https://doi.org/10.26599/NR.2026.94908667

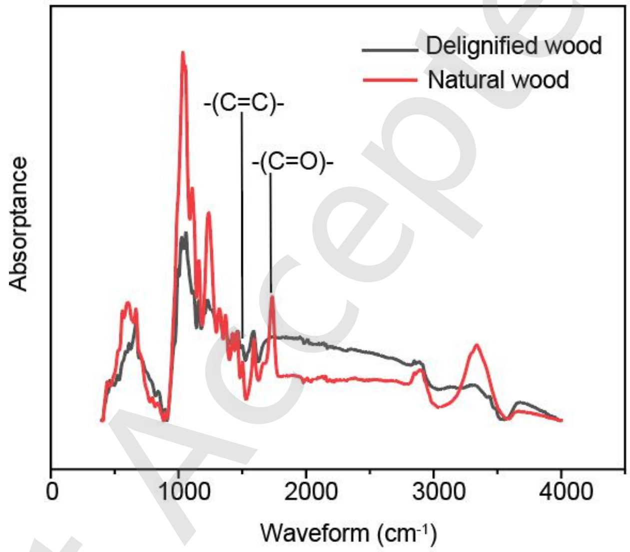

**Fig.S1** FTIR spectra of natural wood and delignified wood.

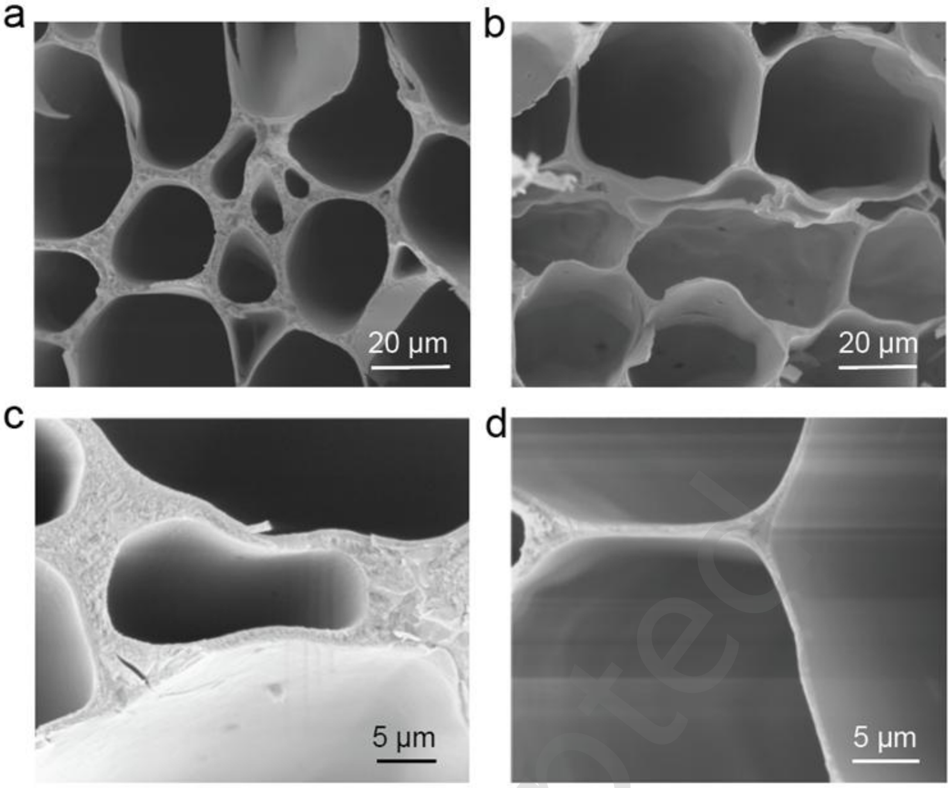

**Fig. S2** SEM images of the (a) upper and (b) lower surfaces of the wood sample and (c-d) the corresponding high-magnification SEM images.

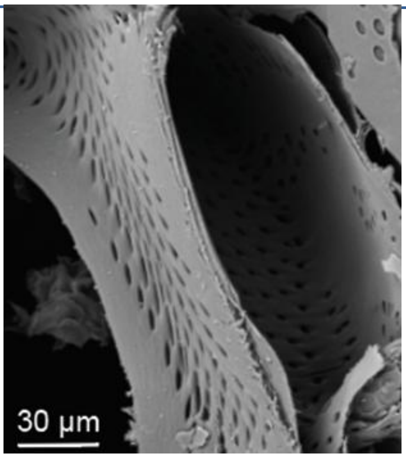

**Fig. S3** High-magnification SEM image showing nano-scale pores distributed on the wood channel wall, forming a hierarchical porous structure.

**Fig. S4** Dynamic wetting behavior of a water droplet on the surface of natural balsa wood. Sequential snapshots at 0, 22, 41, and 57 ms show the rapid penetration of the droplet into the natural wood structure, indicating the intrinsic hydrophilicity and high liquid absorption capability of untreated balsa wood.

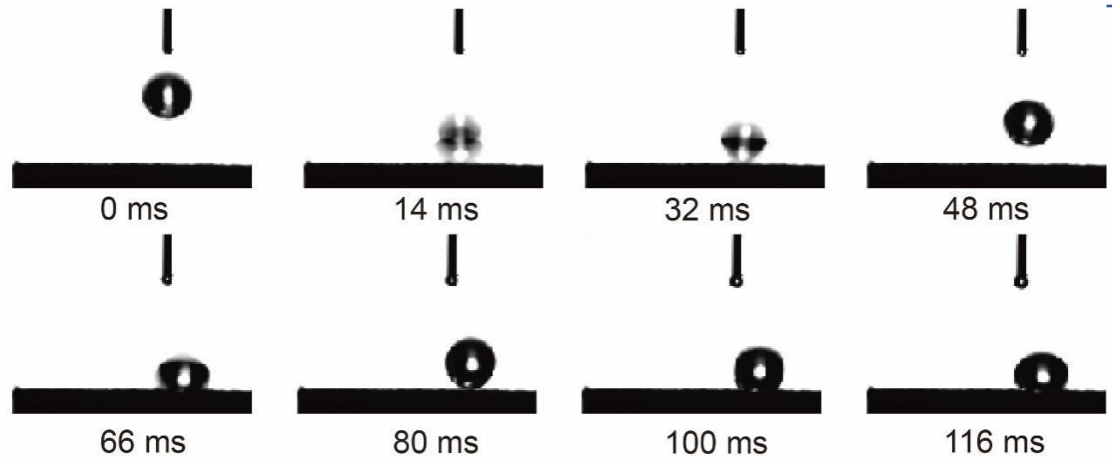

**Fig S5** Dynamic wetting behavior of a water droplet on balsa wood treated with fluorinated graphene. Time-resolved snapshots (0-116 ms) show that the droplet maintains a nearly spherical shape with minimal spreading, demonstrating the enhanced hydrophobicity and suppressed liquid penetration resulting from the fluorinated graphene coating.

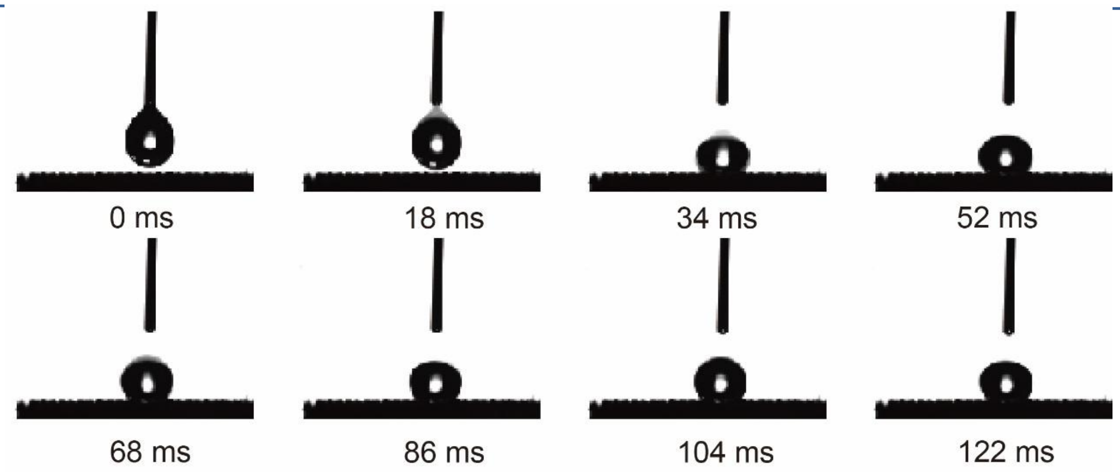

**Fig. S6** Dynamic contact-angle behavior of fluorinated graphene–treated balsa wood with surface-imprinted microstructures. Time-sequenced images (0-122 ms) illustrate the stable droplet shape and minimal spreading upon impact, demonstrating the synergistic enhancement of hydrophobicity provided by the fluorinated coating and the microstructured surface.

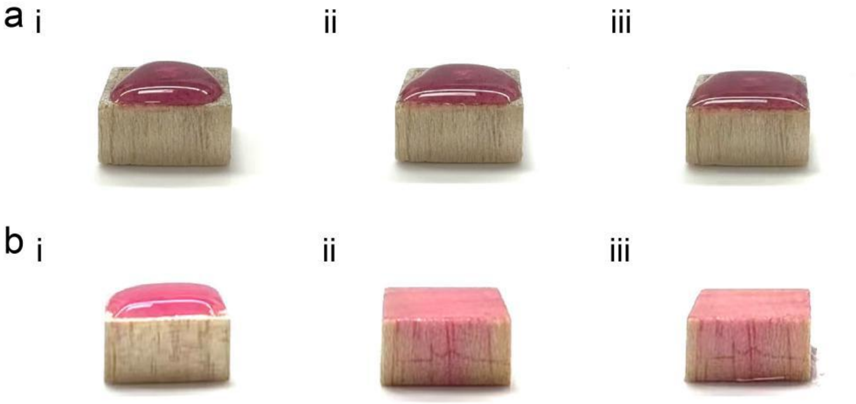

**Fig. S7** Dynamic wetting behavior of the Janus wood surface. (a) Hydrophobic side, where the droplet maintains its shape without noticeable penetration. (b) Hydrophilic side, where the droplet gradually spreads and infiltrates into the wood substrate.

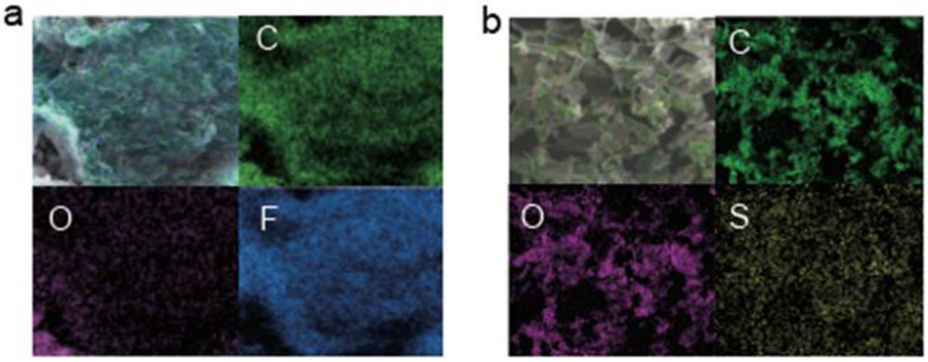

**Fig. S8** EDS elemental mapping of (a) fluorinated graphene-coated wood surface and (b) PSS-modified wood.

**Table S1** Comparison of zeta potential measurements for natural wood, PSS-modified substrate, and fluorinated graphene-coated surface.

| Samples | ζ1 | ζ2 | Mean |
|---|---|---|---|
| Natural wood | -29.4 | -29.2 | -29.3 |
| PSS-modified wood | -37.9 | -38 | -37.95 |
| Fluorinated Graphene-covered surface | -19.3 | -19 | -19.15 |

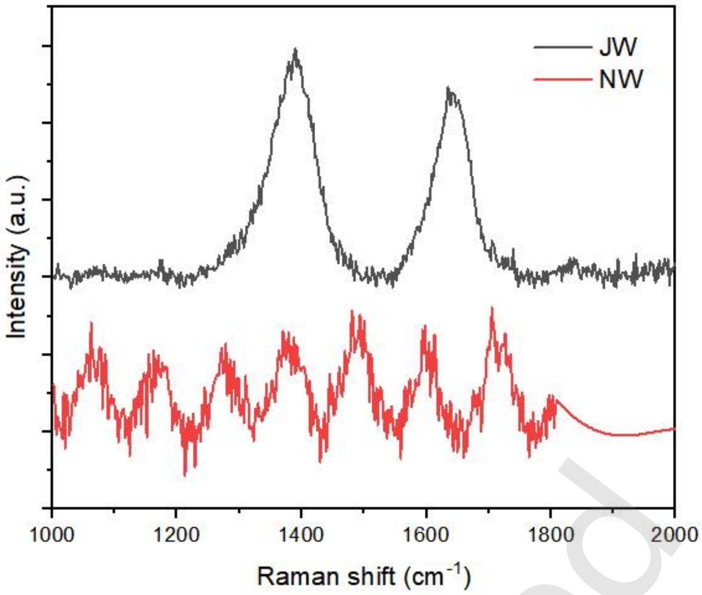

**Fig. S9** Raman spectra of Janus wood (JW) and natural wood (NW) in the range of 1000-2000 cm$^{-1}$. JW exhibits two prominent characteristic peaks associated with the fluorinated modification layer, while NW shows only weak and broad signals, indicating the absence of these structural features.

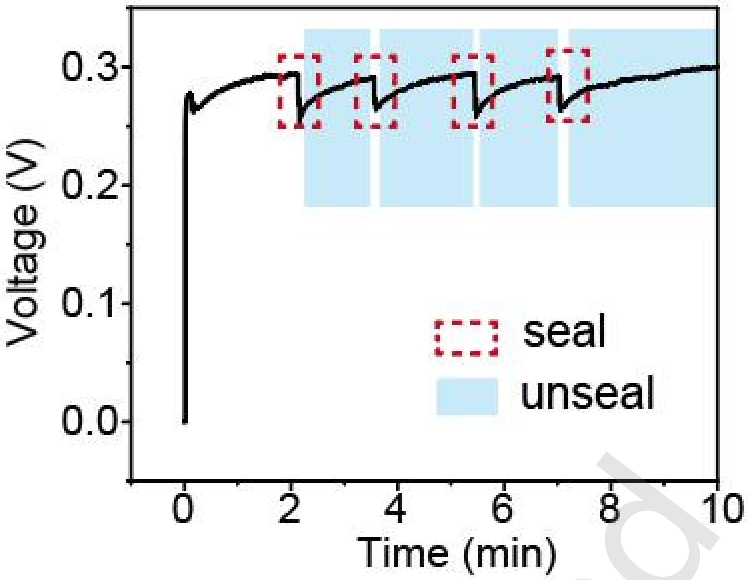

**Fig. S10** Output voltage response of the wood-based hydrovoltaic device under repeated sealing and unsealing cycles. Periodic sealing (red dashed regions) leads to an instantaneous voltage drop due to suppressed evaporation, while unsealing (blue-shaded regions) restores interfacial evaporation and recovers the voltage output. The stable and reversible switching confirms the robustness and environmental responsiveness of the device.

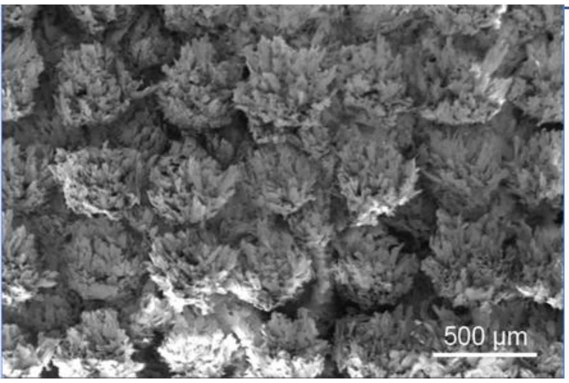

**Fig. S11** SEM image of the surface morphology after long-term operation. The microstructured architecture remains well preserved without structural degradation.

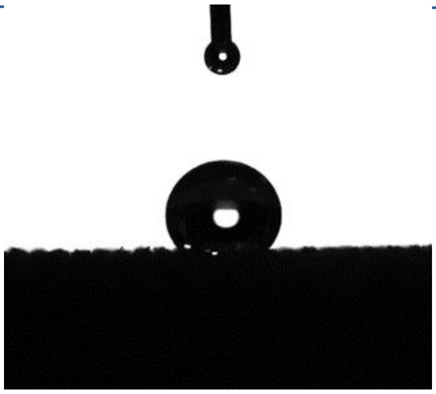

**Fig. S12** Contact angle image of the modified wood surface after long-term operation.

**Table S2** Comparison of zeta potential of the PSS-modified substrate before and after long-term stability testing.

| Samples | ζ1 | ζ2 | Mean |
|---|---|---|---|
| Before long- term operation | -37.9 | -38 | -37.95 |
| After long- term operation | -36.6 | -37.8 | -37.2 |

**Table S3** Performance comparison of open-circuit voltage and short-circuit current between previously reported wood-based WEG systems and the present work.

| | Open-circuit voltage/mV | Short-circuit current/μA |
|---|---|---|
| Ref [1] | 300 | 10 |
| Ref [2] | 96 | 10.5 |
| Ref [3] | 320 | 0.3 |
| Ref [4] | 22.6 | 145 |
| Ref [5] | 27 | 7.5 |
| Ref [6] | 136 | 0.156 |
| Ref [7] | 117.6 | 9700 |
| Our work | 400 | 32 |

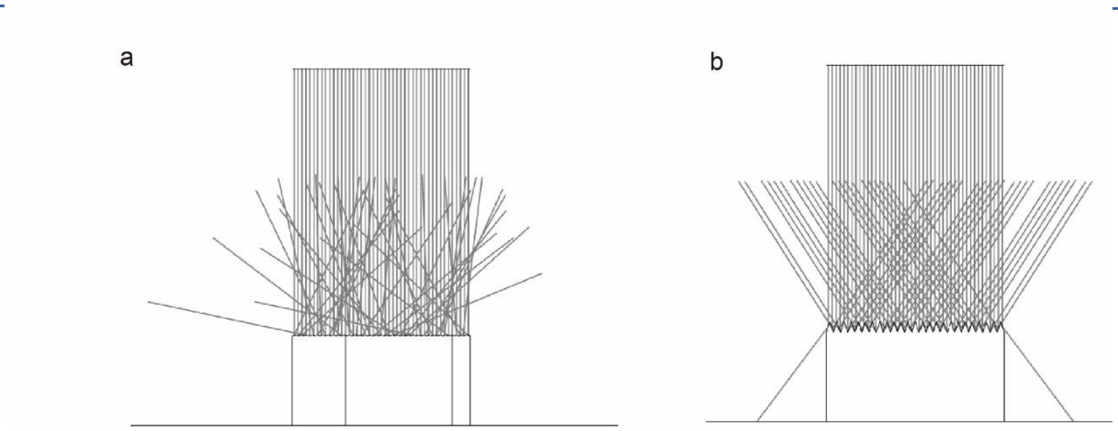

**Fig. S13** Ray-tracing simulation of light propagation atop wood substrates. (a) Natural wood (NW) shows predominantly random reflection and rapid photon escape due to its relatively flat surface. (b) Microstructured wood with an embossed cone-array surface exhibits strong multi-reflection, resulting in prolonged optical confinement within the surface layer.

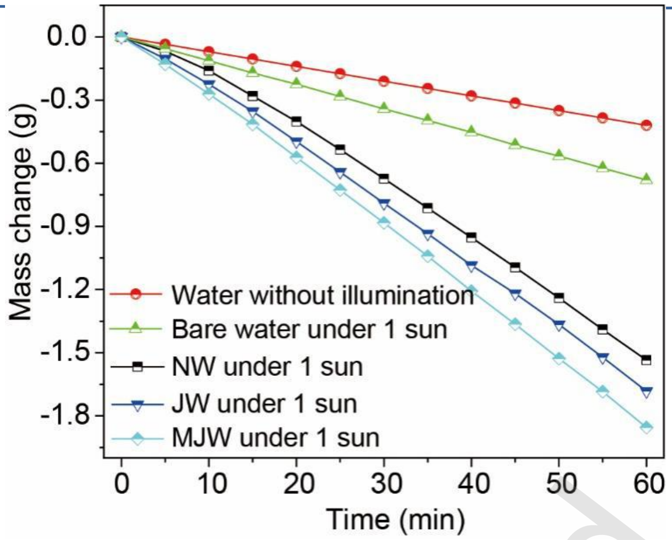

**Fig. S14** Mass change of water over 60 min under different conditions. The red and green curves correspond to water without illumination and bare water under 1 sun, respectively. The black, blue, and cyan curves represent NW (natural wood), JW (Janus wood), and MJW (microstructured Janus wood) placed on the water surface under 1 sun irradiation. The microstructured Janus wood exhibits the fastest mass loss, indicating significantly enhanced interfacial evaporation performance.

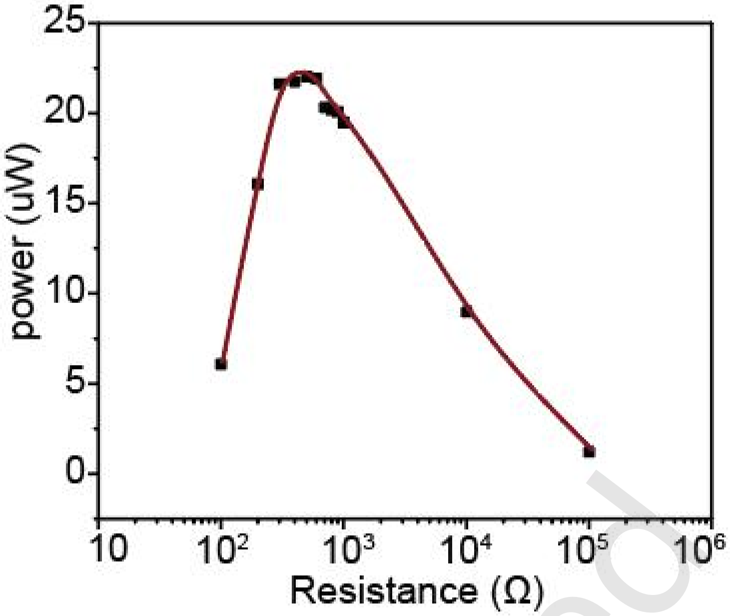

**Fig. S15** Output power as a function of external load resistance for the wood-based evaporation-driven electricity generator equipped with heterogeneous electrodes (aluminum bottom electrode and titanium top electrode). The device exhibits a maximum output power of ~22-23 μW at an optimal load of approximately 500 Ω, after which the power decreases with increasing resistance.

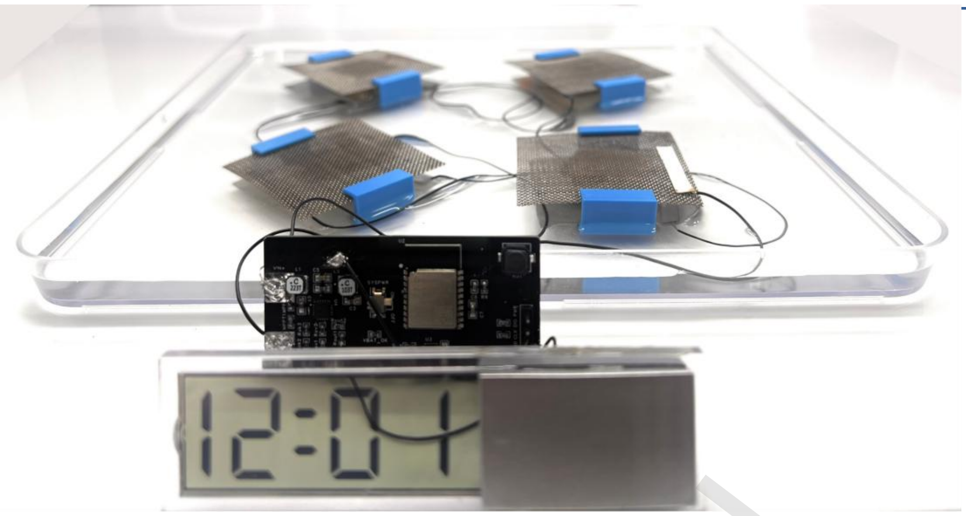

**Fig. S16** Demonstration of the wood-based evaporation-driven generators powering a digital clock.

## References:

Ref [1]: Zhou, X.; Zhang, W.; Zhang, C.; Tan, Y.; Guo, J.; Sun, Z.; Deng, X. Harvesting Electricity from Water Evaporation through Microchannels of Natural Wood. ACS Applied Materials & Interfaces 2020, 12 (9), 11232-11239. DOI: 10.1021/acsami.9b23380.

Ref [2]: Zhang, Z.; Zheng, Y.; Jiang, N.; Hong, W.; Liu, T.; Jiang, H.; Hu, Y.; Li, C. Electricity generation from water evaporation through highly conductive carbonized wood with abundant hydroxyls. Sustainable Energy & Fuels 2022, 6 (9), 2249-2255, 10.1039/D2SE00309K. DOI: 10.1039/D2SE00309K.

Ref [3]: Li, X.; Zhang, K.; Nilghaz, A.; Chen, G.; Tian, J. A green and sustainable water evaporation-induced electricity generator with woody biochar. Nano Energy 2023, 112, 108491. DOI: https://doi.org/10.1016/j.nanoen.2023.108491.

Ref [4]: Li, Z.; Chen, D.; Gao, H.; Xie, H.; Yu, W. Reduced graphene oxide composite nanowood for solar-driven interfacial evaporation and electricity generation. Applied Thermal Engineering 2023, 223, 119985. DOI: https://doi.org/10.1016/j.applthermaleng.2023.119985.

Ref [5]: Lu, W.; Jiang, D.; Wang, Z.; Zhang, X.; Ding, Q.; Zhang, Z.; Liu, X.; Bai, L.; Li, Z.; Liu, Y. Simultaneous efficient evaporation and stable electricity generation enabled by a wooden evaporator based on composite photothermal effect. Chemical Engineering Journal 2024, 496, 154361. DOI: https://doi.org/10.1016/j.cej.2024.154361.

Ref [6]: Jing, M.; Wang, W.; Fu, Y.; Yang, Y.; Song, W.; Sun, Z. A simple, natural 3D honeycomb structure achieving high photothermal conversion and sustainable salt-resistance for efficient desalination and potential electricity generation. Desalination 2023, 564, 116792. DOI: https://doi.org/10.1016/j.desal.2023.116792.

Ref [7]: Ma, C.; An, X.; Guo, M. Superior anti-fouling Janus wood-based evaporator simultaneously achieving efficient evaporation and stable thermoelectric generation. Journal of Cleaner Production 2025, 524, 146513. DOI: https://doi.org/10.1016/j.jclepro.2025.146513.